Phonon-mediated superconductivity in aluminum-deposited graphene AlC$_8$

Hong-Yan Lu [1,*], Yang Yang,[2] Lei Hao [3], Wan-Sheng Wang,[4] Lei Geng,[1] Mengmeng Zheng,[1] Yan Li,[1] Na Jiao,[1]
Ping Zhang,[1,5,†] and C. S. Ting[6]

[1]*School of Physics and Physical Engineering, Qufu Normal University, Qufu 273165, China*
[2]*College of Physics and Electronic Engineering, Zhengzhou University of Light Industry, Zhengzhou 450002, China*
[3]*Department of Physics, Southeast University, Nanjing 210096, China*
[4]*Department of Physics, Ningbo University, Ningbo 315211, China*
[5]*Institute of Applied Physics and Computational Mathematics, Beijing 100088, China*
[6]*Texas Center for Superconductivity and Department of Physics, University of Houston, Houston, Texas 77204, USA*

It has been theoretically predicted and experimentally confirmed that graphene deposited with atoms of a univalent alkali metal such as Li (LiC$_6$) or divalent alkaline-earth metal such as Ca (CaC$_6$) can be a superconductor. For atoms of a trivalent metal such as Al, if deposited on graphene, it was predicted that AlC$_8$ can be in a metallic state. Whether this compound is stable and can be made superconducting is an issue which has not been addressed and deserves further investigation. In this work, based on first-principles calculations, it is found that the phonon spectrum of AlC$_8$ shows imaginary frequencies for the two lowest branches, indicating the structure is dynamically unstable. By hole doping, the imaginary frequencies basically disappear and the lattice is stabilized. Besides, biaxial tensile strain was applied to study its effect on phonon and electron-phonon coupling. With the increase of tensile strain, the high-energy phonon spectrum associated with the C-C stretching modes softens greatly and the electron-phonon coupling becomes stronger, resulting in the increase of superconducting transition temperature T_c to a value of more than 22 K for a sample at the experimentally accessible hole doping (7.5×10^{13} cm^{-2}) and tensile strain (12%) levels. This is above the liquid hydrogen temperature of 20.3 K. Thus, besides Li and Ca deposited graphene, AlC$_8$ provides another platform for realizing superconductivity in graphene.

I. INTRODUCTION

Graphene, a single layer of carbon atoms in a honeycomb lattice, has attracted tremendous attention ever since it was successfully isolated in 2004 [1]. It exhibits many extraordinary properties and has possible potential for a wide range of applications [2–6]. Among the various properties of graphene, superconductivity is one of the most notable expectations. If realized, it may not only be of scientific importance, but may also have good applications in constructing nano-superconducting devices. Recently, superconductivity up to 1.7 K has been reported in magic angle bilayer graphene [7,8], i.e., the two layers of graphene are twisted by a small angle of 1.1°, which may be an unconventional superconductor originating from the strong correlation effect of the interlayer interactions, with the mechanism still hotly debated. How to make monolayer graphene superconducting has also been a hot topic in recent years.

Due to the vanishing electronic density of states (DOS) at the Dirac point, pristine graphene cannot be a superconductor. Doping can induce more charge carriers in graphene by applying electrolytic gating [9,10] or chemical adsorption [11].

For doped graphene, various superconducting pairing mechanisms have been predicted, e.g., plasma-mediated superconductivity [12], resonant-valence-bond paring superconductivity [13], and repulsive electron-electron interaction induced chiral superconductivity [14]. While all these mechanisms may result in possible superconductivity in graphene, phonon-mediated superconductivity is also a probable case [15]. It is known that phonon-mediated superconductivity can be induced with an effective electron-phonon coupling λ, with $\lambda = N(0)D^2/M\omega_{\mathrm{ph}}^2$, where $N(0)$ is the electronic DOS per spin at the Fermi level, D is the deformation potential, M is the effective atomic mass, and ω_{ph} is the frequency of the phonon vibrations involved in superconductivity. Thus, although pristine graphene is not superconducting, it may be a phonon-mediated superconductor with the enhancement of electron-phonon coupling caused by a large number of carriers, strong deformation potential, and strong coupling between electrons and phonon modes.

In a similar case, graphite is also not a superconductor due to the small DOS at the Fermi level. However, it has been known for some time that phonon-mediated superconductivity has been experimentally realized in graphite-intercalated compounds (GICs) such as YbC$_6$ and CaC$_6$ with superconducting transition temperature (T_c) of 6.5 K and 11.5 K, respectively [16,17]. The origin of superconductivity in GICs has mainly been attributed to the formation of an interlayer

_____

*Corresponding author: hylu@qfnu.edu.cn
†Corresponding author: zhang_ping@iapcm.ac.cn

electronic band at the Fermi level, which is formed from the intercalants [18,19]. The interlayer state has multiple beneficial effects on λ: (i) the increase of electron concentration, (ii) the enhanced coupling to carbon out-of-plane vibration, and (iii) the occurrence of the coupling to intercalant in-plane vibrations with the enhancement of deformation potential D and the reduction of $M\omega_{ph}^2$. All these effects lead to the enhancement of λ and consequently the occurrence of superconductivity. Following this guideline, for monolayer graphene, it is anticipated that decorating graphene with electropositive elements shifts the Fermi energy away from the Dirac points, and thus enhances the electron-phonon coupling that might induce superconductivity in the sample.

Actually, it has been theoretically predicted that alkali metal Li or alkaline-earth metal Ca deposited graphene, i.e., LiC_6 and CaC_6, can be a superconductor with T_c of 8.1 K or 1.4 K, respectively [20]. Experimentally, based on angle-resolved photoemission spectroscopy (ARPES) measurements, Fedorov *et al.* evaluated the electronic band structure and extracted the Eliashberg functions of graphene deposited with Cs, K, Na, Rb, Li, and Ca [21]. The authors found universal donor-dependent vibrational modes, and estimated T_c for all these compounds. They pointed out that Ca-deposited graphene is the most promising candidate for superconductivity with the highest T_c approximately equal to 1.5 K. Later, Ludbrook *et al.* reported the ARPES evidence for a superconducting gap in Li-deposited graphene with an estimated T_c of 5.9 K based on the BCS gap equation [22]. Moreover, it was theoretically investigated that the application of strain on Li-deposited graphene can enhance T_c to 29 K [23].

Till now, only the superconductivities in univalent alkali metal atoms and divalent alkaline-earth metal atoms deposited on graphene have been studied. For atoms of a trivalent metal such as Al, if deposited on graphene, it was predicted that AlC_8 is in the metallic state [24]. Whether this compound is stable and can be made superconducting is an issue which has not been addressed and deserves further investigation. In this work, based on first-principles calculations, it is found that the phonon spectrum of AlC_8 shows imaginary frequencies for the two lowest branches, indicating the structure is dynamically unstable. By hole doping, the imaginary frequencies basically disappear and the lattice is stabilized. Besides, biaxial tensile strain was applied to study its effect on phonon and electron-phonon coupling. With the tensile strain increasing up to 12%, the high-energy phonon spectrum gradually softens and the electron-phonon coupling becomes stronger, resulting in the increase of superconducting transition temperature T_c to more than 22 K, which is higher than the liquid hydrogen temperature of 20.3 K. Thus, AlC_8 could provide another platform for realizing superconductivity in graphene.

It is worth noting that we also studied other stoichiometries of Al and C, such as AlC_6, AlC_{24}, and AlC_{32}, with the lattice structure and the phonon spectra described in Appendix A. For the phonon spectra, they show larger imaginary frequencies than AlC_8, thus are more unstable. Especially, for AlC_6, with the same stoichiometric ratio as LiC_6 and CaC_6 [20–23], stabilization is very difficult whether by doping or applying strain. As a result, it cannot stably exist in reasonable ex-

perimental setups. Therefore, in the following parts, we only discuss the properties of AlC_8.

The rest of this paper is organized as follows. In Sec. II, we describe the computational details. In Sec. III, we present the results and discussions. First, we show how to make the lattice of AlC_8 stable. Second, we discuss the electronic structure, including the band structure, Fermi surface (FS), and DOS of AlC_8 under different circumstances. Third, the phonon and electron-phonon coupling of AlC_8 are calculated and the possible superconducting transition temperature is further calculated. Section IV is the conclusion of the work. In Appendix A, the lattice structure and phonon spectra of AlC_6, AlC_{24}, and AlC_{32} are described. In Appendix B, the Bader charge, electron localization function, and charge density difference of pristine AlC_8 are discussed. In Appendix C, the origin of the lattice instability of AlC_8 is discussed.

II. COMPUTATIONAL DETAILS

The electronic structure calculations of AlC_8 were performed in the framework of the density functional theory as implemented in the QUANTUM ESPRESSO (QE) program [25], and the lattice dynamics was performed within the density functional perturbation theory [26] as implemented in QE. The projector augmented wave method [27] was used to model the electron-ion interactions, and the generalized gradient approximation (GGA) with the Perdew-Burke-Ernzerhof (PBE) parametrization [28] was adopted for the exchange-correlation potentials. It is worth noting that calculations under the PBEsol functional [29] were also performed, with the results basically consistent with those under PBE. Thus, we only show the results under PBE. The Bader charge [30], electron localization function, and charge density difference were calculated using the VASP code [31]. In our calculations, a vacuum space of 20 Å normal to the graphene layer was used to avoid interactions between adjacent layers. Both the lattice parameters and the atom positions were relaxed to obtain the optimized structure. The cutoffs for wave functions and charge density were set as 80 Ry and 480 Ry, respectively. The electronic integration was performed over a $12 \times 12 \times 1$ k-point grid. For FS and DOS calculations, denser $36 \times 36 \times 3$ and $96 \times 96 \times 1$ k-point grids were adopted, respectively. The phonon and electron-phonon coupling were calculated on a $6 \times 6 \times 1$ q-point grid, and a denser $24 \times 24 \times 1$ k-point grid was used for evaluating an accurate electron-phonon interaction matrix.

The electron-phonon coupling properties and possible superconductivity were calculated based on Eliashberg equations [32]. The Eliashberg spectral function $\alpha^2 F(\omega)$ describes the averaged coupling strength between the electrons at the Fermi energy (E_F) and the phonons of energy ω:

$$\alpha^2 F(\omega) = \frac{1}{N(E_F)N_k N_q} \sum_{\mathbf{k},\mathbf{q},\nu,i,j} \left| g_{\mathbf{k}i,\mathbf{k}+\mathbf{q}j}^{\mathbf{q}\nu} \right|^2 \delta(\omega - \omega_{\mathbf{q}\nu})$$
$$\times \delta(\varepsilon_{\mathbf{k}i} - E_F)\delta(\varepsilon_{\mathbf{k}+\mathbf{q}j} - E_F), \quad (1)$$

where $N(E_F)$ is the electronic DOS at the Fermi energy, and N_k and N_q are the total numbers of $\mathbf{k}$ and $\mathbf{q}$ points, respectively. $\omega_{\mathbf{q}\nu}$ is the phonon frequency of the νth phonon mode at vector $\mathbf{q}$, $\varepsilon_{\mathbf{k}i}$ and $\varepsilon_{\mathbf{k}+\mathbf{q}j}$ are eigenvalues of Kohn-

Sham orbitals at given bands and wave vectors, and $g_{\mathbf{k}i,\mathbf{k}+\mathbf{q}j}^{\mathbf{q}\nu}$ is the electron-phonon coupling matrix element. Then, the frequency-dependent electron-phonon coupling $\lambda(\omega)$ can be obtained by

$$\lambda(\omega) = 2 \int_0^\omega \frac{\alpha^2 F(\omega')}{\omega'} d\omega', \tag{2}$$

and the total electron-phonon coupling λ can be obtained when $\omega \to \infty$.

Using the Allen-Dynes modified McMillan equation [33], the superconducting transition temperature can be evaluated as follows:

$$T_c = \frac{\omega_{\log}}{1.2} \exp\left[-\frac{1.04(1+\lambda)}{\lambda - \mu^*(1 + 0.62\lambda)}\right], \tag{3}$$

where μ^* is the Coulomb pseudopotential and was set to a typical value of $\mu^* = 0.1$ in our calculations, and $\omega_{\log}$ is the logarithmically averaged phonon frequency defined as

$$\omega_{\log} = \exp\left[\frac{2}{\lambda} \int \frac{\alpha^2 F(\omega) \log \omega}{\omega} d\omega\right]. \tag{4}$$

III. RESULTS AND DISCUSSION

A. Lattice structure and stability

For AlC_8, we first calculated the total energy of hollow, top, and bridge coverages of the Al atom on graphene, with the Al atom lying above the center of the hexagon formed by the six C atoms, above the C atom, and above the center of the C-C bond, respectively. It is found that $E_{\text{hollow}} < E_{\text{bridge}} < E_{\text{top}}$, with the total energy of the bridge and top coverages 0.11 eV/unit cell and 0.13 eV/unit cell higher than that of the hollow coverage, respectively. Thus, we only study the energetically most favorable hollow coverage of AlC_8. The lattice structure for it is shown in Fig. 1(a), where yellow (purple) spheres represent C (Al) atoms. In the unit cell, there are eight C atoms and one Al atom, with the Al atom lying at the hollow position, which can be clearly seen from the side view of the AlC_8 unit cell in Fig. 1(b). Here h is the distance between the Al atom and the graphene plane. In the AlC_8 unit cell, there are two kinds of C-C bond lengths with different values. One is labeled as l_1, which represents the C-C bond lengths in the hexagon under Al atom. The other is labeled as l_2, corresponding to the length of other C-C bonds. The lengths of the parameters under different circumstances can be obtained after fully structural optimization.

The optimized structural parameters of AlC_8 can be obtained, which are shown in Table I. The Al-graphene distance h is 2.097 Å, and the C-C bond lengths l_1 and l_2 are 1.438 and 1.429 Å, respectively. The distance between Al and the nearest C atoms is 2.542 Å. To know whether Al atom forms bonds with the nearest C atoms, we first did total energy calculation, and found that the total energy of AlC_8 is 1.08 eV/unit cell lower than that of a free Al atom plus eight C atoms in graphene, indicating that AlC_8 is thermodynamically stable. Then, the Bader charge, electron localization function, and charge density difference are calculated, together proving that the Al atom loses electrons and forms Al-C bonds with the graphene plane (the results are shown in Appendix B). To make this clear, we define this state as pristine AlC_8, in com-
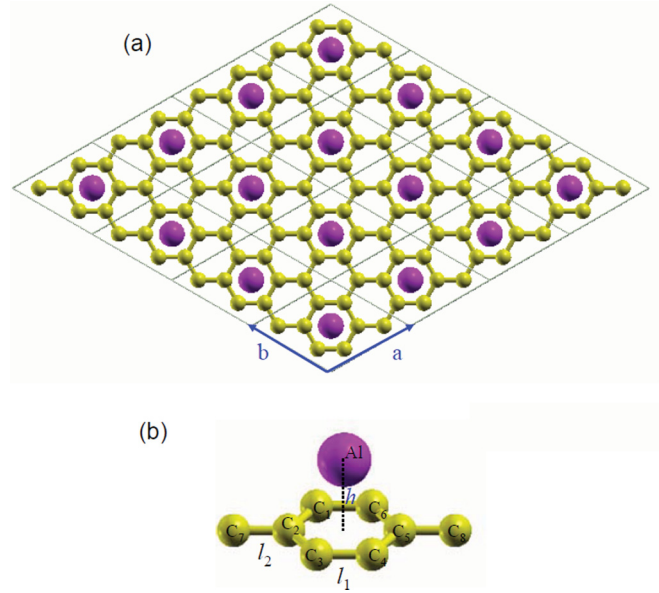

FIG. 1. (a) Periodic structure of aluminum-deposited graphene AlC_8. Yellow (purple) spheres represent carbon (aluminum) atoms. (b) Side view of the AlC_8 unit cell. h is the distance between Al atom and the graphene plane. l_1 and l_2 are two different C-C bond lengths in AlC_8 lattice. All the atoms in the unit cell are labeled to facilitate the description of Bader charges of the atoms.

parison with the otherwise hole-doped and stretched states based on this, which will be discussed later. Moreover, with the same coverage as AlC_8, we considered the full relaxation of supercells such as Al_4C_{32}, and no distortion was found, supporting the rationality of the AlC_8 lattice structure.

Based on the relaxed structure of pristine AlC_8, we calculated the phonon spectrum for it, with the result shown in Fig. 2(a). It is seen that two branches show imaginary frequencies with the maximum of -57.5 cm^{-1} at the K point (the imaginary frequencies were plotted as a negative value following the conventional notation), indicating that the pristine AlC_8 is dynamically unstable. It is known that doping or tensile strain can be applied to stabilize phonons and induce superconductivity in several systems, for example, in

TABLE I. Optimized structural parameters (Al-graphene distance h, C-C bond lengths l_1 and l_2, in Å), the maximum of phonon spectrum $\omega_{\max}$ and logarithmic frequency average $\omega_{\log}$ in cm^{-1}, electron-phonon coupling λ and superconducting critical temperature T_c for pristine or hole-doped and stretched states. p is the hole doping level in $|e|$/unit cell, and ε is the effect of tensile strain, i.e., the relative increase of the lattice constant.

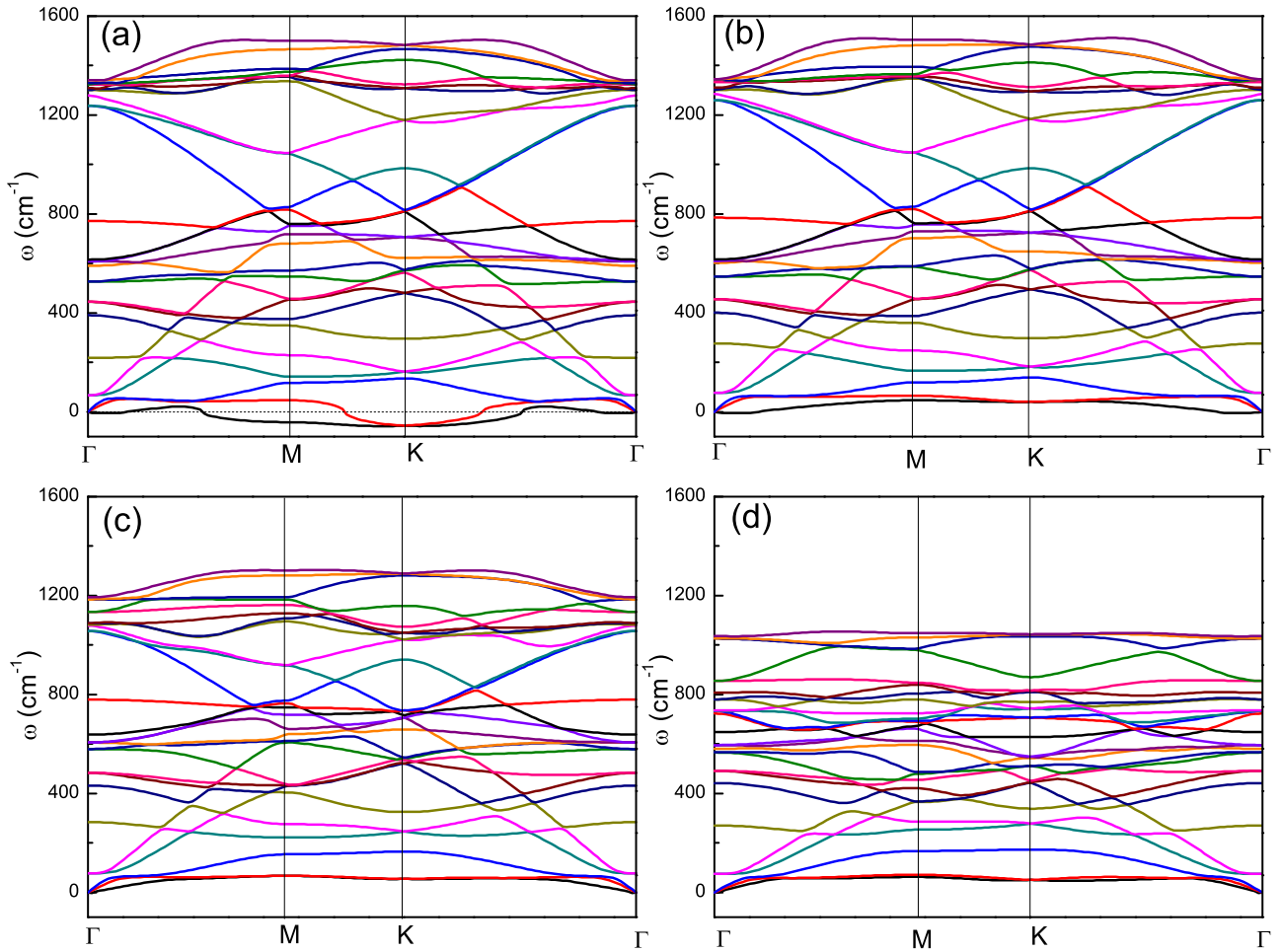| p	ε	h	l_1	l_2	$\omega_{\max}$	$\omega_{\log}$	λ	T_c
0	0	2.097	1.438	1.429	1504			
0.2	2%	2.080	1.467	1.457	1403	306.064	0.644	8.577
0.2	4%	2.074	1.496	1.485	1303	326.249	0.655	9.558
0.2	6%	2.069	1.526	1.513	1212	302.015	0.738	11.893
0.2	8%	2.063	1.556	1.539	1127	281.587	0.798	13.113
0.2	10%	2.057	1.587	1.567	1054	322.790	0.917	19.535
0.2	12%	2.049	1.618	1.593	994	188.452	1.557	22.234

FIG. 2. Phonon spectra of AlC_8 along high-symmetry line Γ-M-K-Γ in (a) pristine state, (b) hole-doped and strain-free state ($p = 0.2$), (c) hole-doped and slightly stretched state ($p = 0.2$, $\varepsilon = 4\%$), and (d) hole-doped and significantly stretched state ($p = 0.2$, $\varepsilon = 10\%$).

N- or B-doped graphene [34], $1T$-TaS_2 [35], two-dimensional boron [36], etc. Compared with the stable LiC_6 and CaC_6, the dynamical instability of AlC_8 may arise from the abundant electrons provided by Al atoms. Thus, hole doping to the system may make it stable. Here we define hole doping level p in units of $|e|$/unit cell. It is found that with p increasing from zero, the imaginary frequencies become less obvious. When p is $0.2|e|$/unit cell, the imaginary frequencies of the phonon spectrum basically disappear [Fig. 2(b)]. Around the Γ point, the lowest phonon branch, which corresponds to the out-of-plane transverse acoustic mode (the so-called ZA mode or flexural phonon mode), shows a very small imaginary frequency, i.e., about -4 cm^{-1}. This is due to the difficulty of achieving numerical convergence for the flexural phonon mode and can disappear completely under certain cases, which appears to be a common issue in first-principles calculations for two-dimensional materials [37,38]. Therefore, the phonon spectrum suggests that AlC_8 at $p = 0.2$ hole doping is dynamically stable. For comparison, the phonon spectra for electron-doped cases with electron doping levels of $-0.1|e|$/unit cell and $-0.2|e|$/unit cell were calculated, and imaginary frequencies of -75.4 cm^{-1} and -85.6 cm^{-1} were found, suggesting that the system is even more unstable. Thus, we only consider the hole-doped case.

Furthermore, biaxial tensile strain was applied to study its effect on phonon and electron-phonon coupling. It was applied along the two basis vector directions, and the relative increase of lattice constant was defined as $\varepsilon = (a - a_0)/a_0$, where a_0 and a are the lattice constants of unstretched and stretched AlC_8, respectively. Figures 2(c) and 2(d) show the phonon spectra in the hole-doped and slightly stretched state ($p = 0.2$, $\varepsilon = 4\%$), as well as in the hole-doped and significantly stretched state ($p = 0.2$, $\varepsilon = 10\%$). It is seen that tensile strain can make the lowest branch around Γ more dispersive and the high-energy phonon spectra greatly softened. Strains larger than 13% are not applied due to the reappearance of structural instability (in Appendix C, the origin of the lattice instability for the pristine and $p = 0.2$, $\varepsilon = 15\%$ cases were discussed).

The optimized structural parameters and the maximum of the phonon spectrum ω_{max} for the stable cases are also listed in Table I. It is seen that, for the $p = 0.2$ and stretched cases, with the increase of tensile strain, the Al-graphene distance h decreases, while the C-C bond lengths l_1 and l_2 increase gradually. It is understandable that the tensile strain increases the distance of neighboring C atoms, and the π bonds less repulse the Al atom, which thus moves down toward the graphene plane. According to the equation $\lambda =$
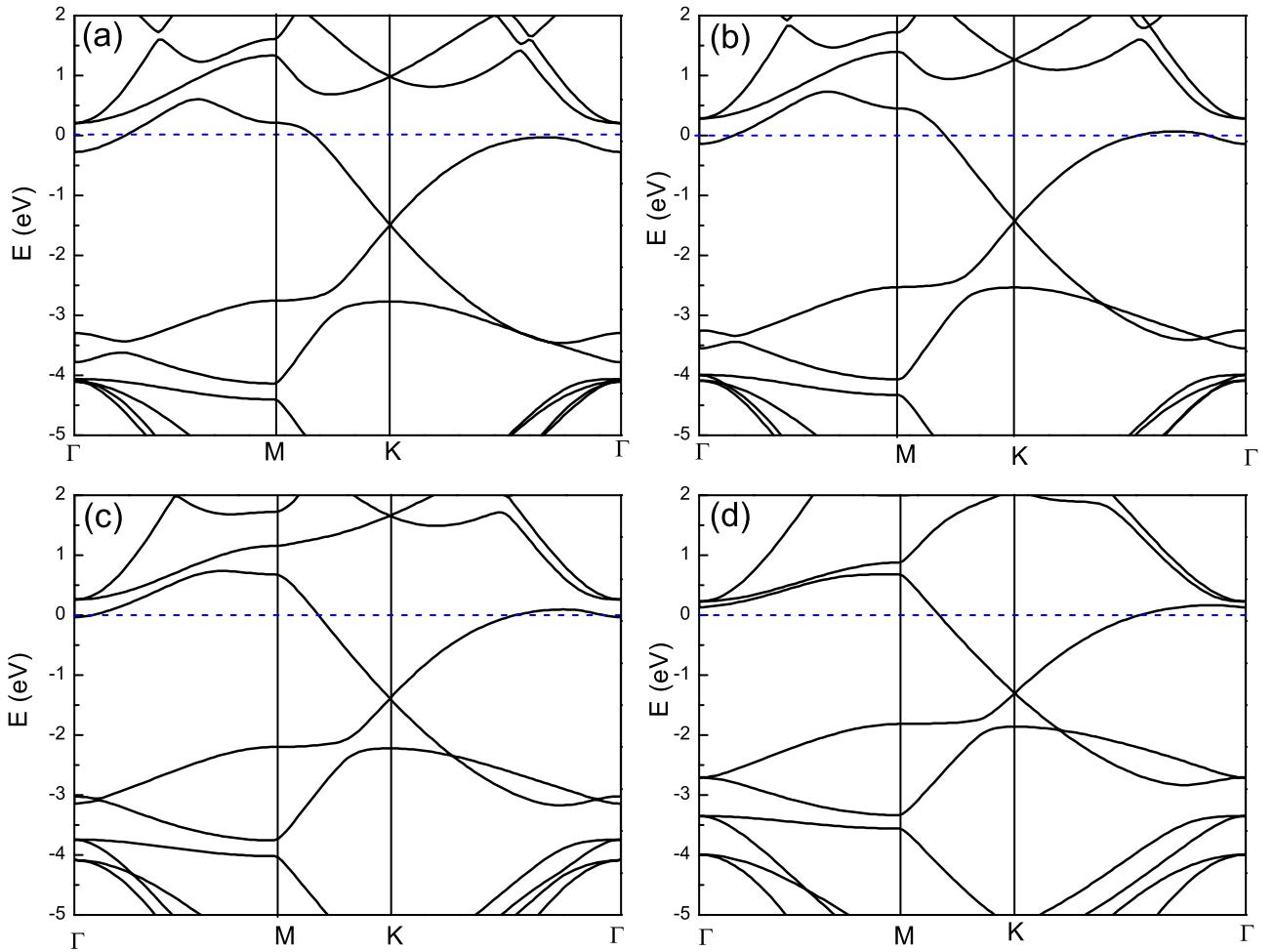
FIG. 3. Electronic band structure of AlC$_8$ along high-symmetry line Γ-M-K-Γ for the four cases listed in Fig. 2, i.e., (a) pristine state, (b) hole-doped and strain-free state ($p = 0.2$), (c) hole-doped and slightly stretched state ($p = 0.2$, $\varepsilon = 4\%$), and (d) hole-doped and significantly stretched state ($p = 0.2$, $\varepsilon = 10\%$). The Fermi level in blue dashed lines is set to be zero.

$N(0)D^2/M\omega_{ph}^2$, with the decrease of Al-graphene distance h, the deformation potential D increases, while the high-energy phonon spectrum softens with the maximum ω_{ph} decreasing from 1504 cm^{-1} to 994 cm^{-1}, both leading to the increase of λ and thus the superconducting transition temperature, which will be discussed later.

B. Electronic structure

For the electronic structure, the band structure, FS, and DOS were studied for different cases. First, the electronic band structure of AlC$_8$ along high-symmetry line Γ-M-K-Γ were calculated for the same cases listed in Fig. 2, with the results shown in Fig. 3. For the pristine AlC$_8$, it is a metal with one band crossing the Fermi level along the Γ-M and M-K directions, consistent with the former result [24]. For the hole-doped and strain-free state of AlC$_8$ ($p = 0.2$), the Fermi level moves downward, and crosses the band twice along K-Γ. By further applying tensile strain, as seen in Figs. 3(c) and 3(d), the shape of the bands changes a little, and the Fermi level still moves downward. Finally, no band crosses the Fermi level along Γ-M and the Fermi level crosses the band only once along K-Γ.

The FSs for the four cases listed in Fig. 3 are plotted in Fig. 4. The FS for the unstable pristine AlC$_8$ can be seen in Fig. 4(a), with six big pieces in the first Brillouin zone (BZ), which originate from the six big hole pockets extended from near the Γ point to slightly beyond the M point [see Fig. 3(a)] in the extended BZ. However, the topology of the FSs changes dramatically for the hole-doped and strained cases. When hole doped, the Fermi level moves downward, making the six pockets become larger and touch each other. At $p = 0.2$, with zero strain, the FSs [see Fig. 4(b)] appear to come from the six big electron pockets around K points and the small electron pocket centered at the Γ point [see Fig. 3(b)]. With the further increase of tensile strain, the electron pocket around Γ shrinks to a smaller circle [Fig. 4(c)] and gradually disappears [Fig. 4(d)], while the six electron pockets around K barely change. The change of FSs in Fig. 4 agrees well with the corresponding band structures in Fig. 3.

Then, we show the electronic DOS for the stable cases. Figure 5(a) shows the total and orbital-projected electronic DOS for hole-doped and slightly stretched AlC$_8$ ($p = 0.2$ and $\varepsilon = 2\%$). At the Fermi level, the DOS is near a van Hove singularity peak. The $2p_x$ and $2p_y$ orbitals of C atoms only contribute to the states below -4 eV and thus were not plotted
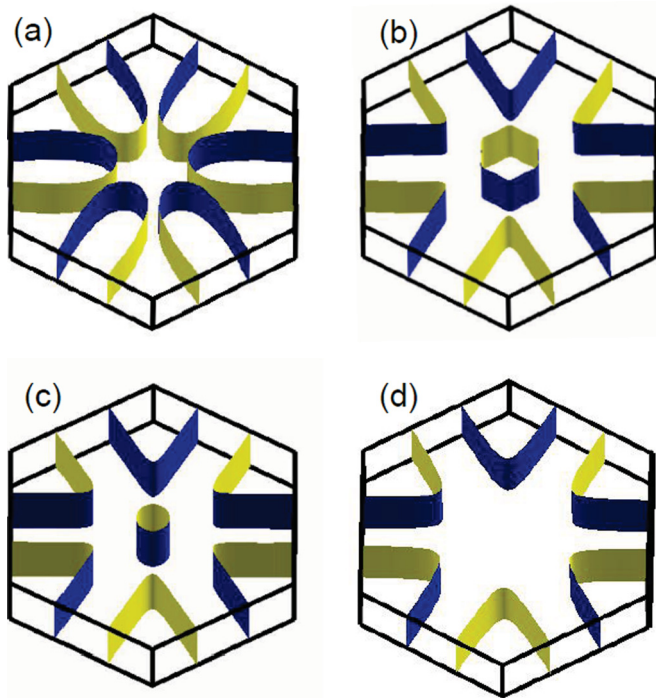
FIG. 4. Fermi surface of AlC$_8$ for the four cases listed in Fig. 3, i.e., (a) pristine state, (b) hole-doped and strain-free state ($p = 0.2$), (c) hole-doped and slightly stretched state ($p = 0.2$, $\varepsilon = 4\%$), and (d) hole-doped and significantly stretched state ($p = 0.2$, $\varepsilon = 10\%$).

in the figure. In the range of -2 eV to 1 eV, the DOS is mainly contributed by the $2p_z$ orbital of C atoms. On the other hand, near the Fermi level, the contribution of the $3p$ orbital of the Al atom is also not negligible, suggesting the formation of Al-C bonds and hybridization between the $2p_z$ orbital of C and $3p$ orbital of Al. Besides, Al contributes greatly for the
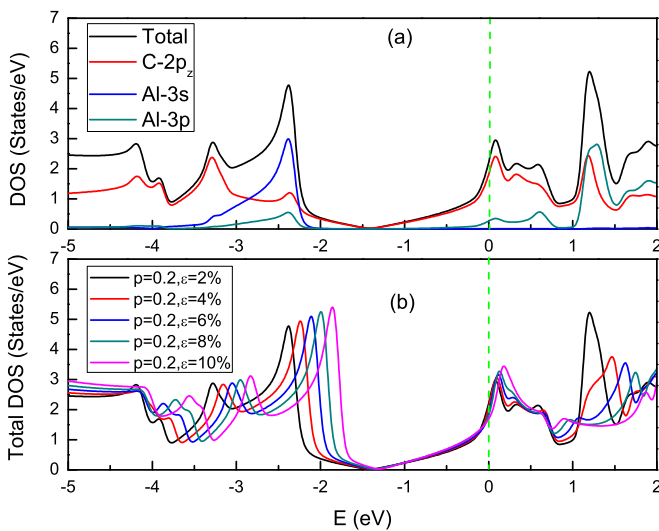
FIG. 5. (a) Total and orbital-projected electronic DOS for hole-doped and slightly stretched AlC$_8$ ($p = 0.2$ and $\varepsilon = 2\%$). (b) Total electronic DOS for five cases: $p = 0.2$ and $\varepsilon = 2\%$, $p = 0.2$ and $\varepsilon = 4\%$, $p = 0.2$ and $\varepsilon = 6\%$, $p = 0.2$ and $\varepsilon = 8\%$, and $p = 0.2$ and $\varepsilon = 10\%$.
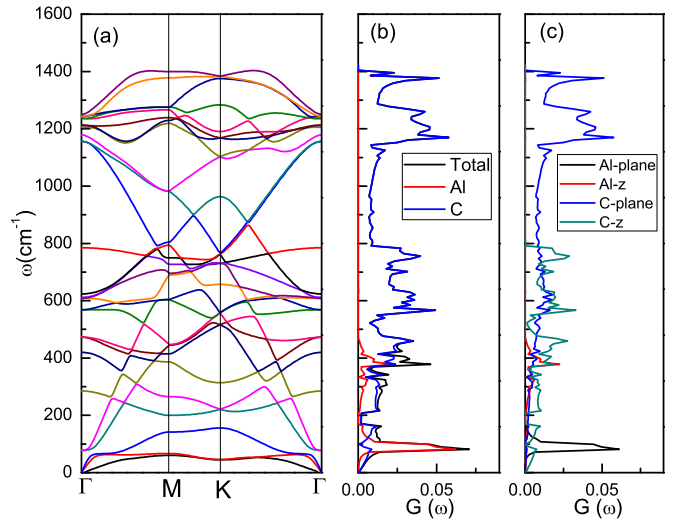

FIG. 6. (a) Phonon spectrum, (b) atom-projected phonon DOS, and (c) direction-projected phonon DOS for Al and C atoms for hole-doped and slightly stretched AlC$_8$ ($p = 0.2$ and $\varepsilon = 2\%$).

electron states above 1 eV and between -3.5 eV to -2 eV. Figure 5(b) shows the effect of tensile strain on the total DOS. With the increase of tensile strain, the total DOS basically moves to higher energy and the total DOS at the Fermi level decreases slightly.

C. Electron-phonon coupling and possible superconductivity

To study the possible phonon-mediated superconductivity in AlC$_8$, the phonon and electron-phonon coupling properties were first studied. For the phonon spectrum and the corresponding vibration information, we took the hole-doped and slightly stretched AlC$_8$ ($p = 0.2$ and $\varepsilon = 2\%$) as an example. The phonon spectrum is shown in Fig. 6(a). There is a wide range of frequency extending up to about 1403 cm^{-1}, and no imaginary frequency appears in the low energy, justifying its dynamical stability. To know more about the atomic vibration information, the atom-projected and direction-projected phonon DOS are plotted in Figs. 6(b) and 6(c). Since the Al atom is heavier than the C atom, the vibration modes at the low-energy range are mainly contributed by Al atoms with a sharp peak near 70 cm^{-1}. The vibration of C atoms contributes to the whole range of energy, and is the only contribution to the modes for energy higher than 450 cm^{-1}. By further checking the direction-projected phonon DOS, it is seen that the peak near 70 cm^{-1} is mostly contributed by the in-plane modes of Al together with a small contribution of C out-of-plane modes; the range of energy between 200 cm^{-1} to 450 cm^{-1} is contributed by the in-plane and out-of-plane modes of C mixed with the out-of-plane modes of Al near 400 cm^{-1}; while that between 450 cm^{-1} to 800 cm^{-1} is contributed by the in-plane and out-of-plane modes of C. Furthermore, the energy higher than 800 cm^{-1} are only contributed by the in-plane C-C stretching modes. For the other cases of doped and stretched AlC$_8$, similar vibration modes can be obtained. The total phonon DOS for different cases is shown in Fig. 7. With the increase of tensile strain, although the low-energy and medium-energy modes barely
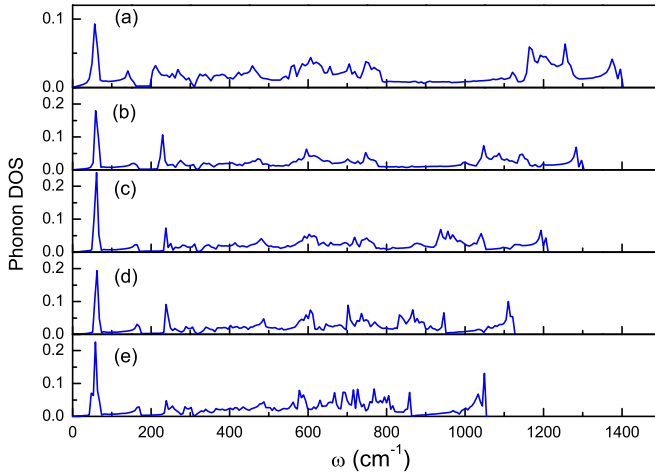
FIG. 7. Total phonon DOS for doped and stretched AlC_8. (a) $p = 0.2$ and $\varepsilon = 2\%$, (b) $p = 0.2$ and $\varepsilon = 4\%$, (c) $p = 0.2$ and $\varepsilon = 6\%$, (d) $p = 0.2$ and $\varepsilon = 8\%$, and (e) $p = 0.2$ and $\varepsilon = 10\%$.

move, there is obvious softening of the high-energy C-C in-plane stretching modes, consistent with previous results in pure graphene [39], doped graphene [15,40], and Li-deposited graphene [23]. As we will show in what follows, this greatly increases the electron-phonon coupling.

Then, we discuss the Eliashberg spectral function $\alpha^2 F(\omega)$ and electron-phonon coupling $\lambda(\omega)$ for different cases, with the results shown in Fig. 8. It is seen that the position of the peaks in the Eliashberg spectral function resembles that of the total phonon DOS. The low-energy peak of the Eliashberg spectral function originates from the coupling between electrons and the low-energy in-plane modes of Al mixed with a small contribution of C out-of-plane modes, which contributes to about half of the total electron-phonon coupling λ. The other major contribution is from the coupling between electrons and the high-energy in-plane C-C stretching modes, which contributes to about one-third of the total λ.
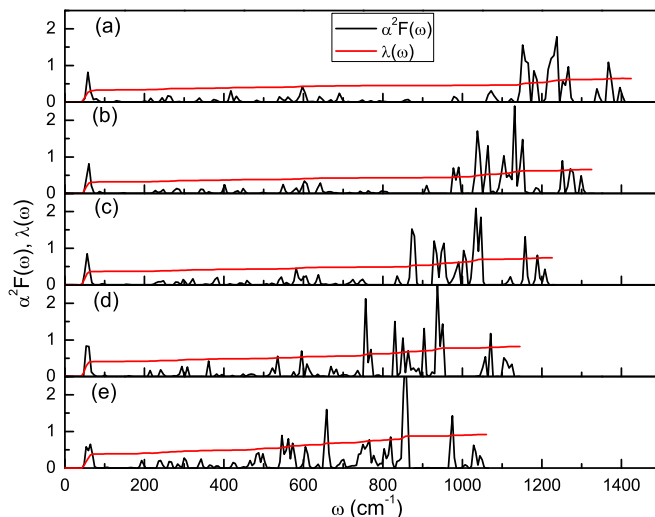

FIG. 8. Eliashberg spectral function $\alpha^2 F(\omega)$ and electron-phonon coupling $\lambda(\omega)$ for the same cases as in Fig. 7.

Based on the Eliashberg spectral function $\alpha^2 F(\omega)$, the total λ and the logarithmically averaged phonon frequency $\omega_{\log}$ can be calculated under different cases. Using the Allen-Dynes modified McMillan equation [33], the superconducting transition temperature can further be evaluated, with the results shown in Table I. It is seen that with the increase of tensile strain, the total electron-phonon coupling λ increases from 0.644 ($p = 0.2$, $\varepsilon = 2\%$) to 1.557 ($p = 0.2$, $\varepsilon = 12\%$), and the corresponding superconducting transition temperature T_c increases from 8.577 K to 22.234 K, which is above the liquid hydrogen temperature of 20.3 K. Thus, Al-deposited graphene AlC_8 provides another platform for realizing superconductivity in graphene.

It is worth mentioning that superconductivity and the increase of T_c in AlC_8 can be realized within the experimentally accessible doping and strain levels. The hole doping level of $0.2|e|$/unit cell for the strained stable cases corresponds to about hole concentration from 7.5×10^{13} cm^{-2} to 9.3×10^{13} cm^{-2}, while the doping level above 10^{14} cm^{-2} in graphene has been achieved for both electrons and holes by electrolytic gating [10] or by chemical adsorption [11]. On the other hand, tensile strain up to about 25% has been elastically applied to graphene without breaking [41]. Therefore, as the realization of superconductivity in LiC_6 and CaC_6, it is highly reasonable to anticipate the experimental realization of superconductivity in Al-deposited graphene AlC_8.

Before concluding, we make some comparisons with previous results of superconductivity in graphene with/without metal deposition, under doping and/or strain. As has been mentioned, graphene deposited with Li or Ca can be a superconductor with T_c lower than 10 K [20–22]. The application of strain on Li-deposited graphene can enhance T_c to 29 K [23]. Our investigation shows that graphene deposited with Al can also be a superconductor with T_c about 22 K under hole doping and tensile strain. There is also an interesting work investigating the combined effect of charge doping and biaxial tensile strain on graphene, which can increase T_c to about 30 K. Since there are no other atoms involved, it was called "intrinsic superconductivity" [15]. The above results reveal that the deposition of metal on graphene induces metal-related electronic states, which not only increases the electron concentration, but also enhances the coupling with both the low-energy in-plane vibrations of metal atoms and the out-of-plane vibrations of carbon atoms. This is important because in doped graphene with no metal on it, symmetry forbids the coupling between π states and the out-of-plane vibrations of carbon atoms; meanwhile, the coupling with the in-plane vibrations is not large enough and thus λ is small. Therefore, the deposition of metal improves this greatly, similarly to the role of metal in GICs [18,19,42].

Moreover, for the effect of strain on superconductivity of graphene, our work and Refs. [15,23] prove that it can soften the high-energy in-plane C-C stretching modes, further increasing the electron-phonon coupling and T_c. Besides, there were also works based on theoretical models studying strain-induced superconductivity in graphene, for example, superconducting states in pseudo-Landau-levels [43], time-reversal odd superconductivity [44], flat-band superconductivity [45], and superconducting pair density wave states [46]. Based on
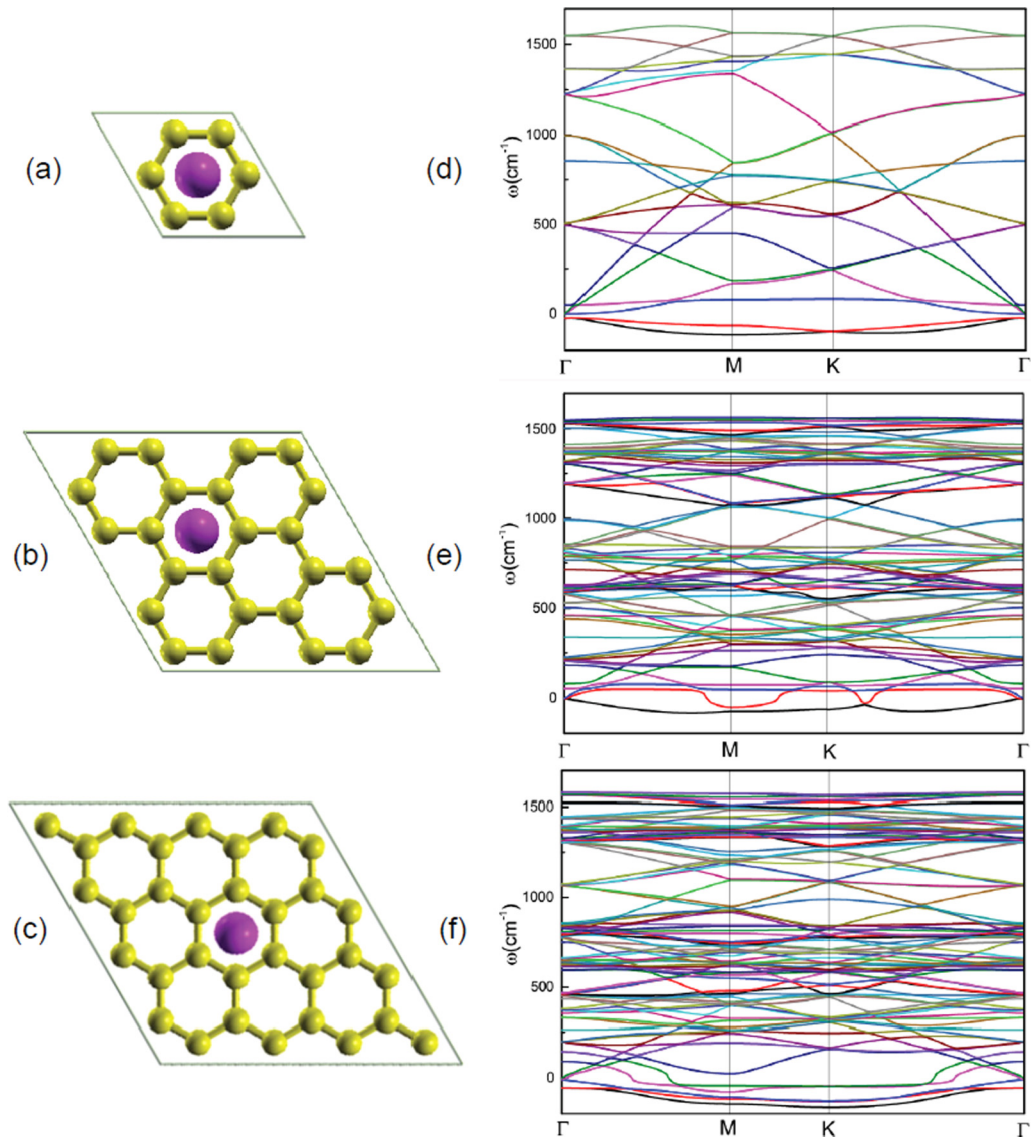
FIG. 9. (a), (b), and (c) are the unit cells of AlC_6, AlC_{24}, and AlC_{32}. (d), (e), and (f) are the phonon spectra for AlC_6, AlC_{24}, and AlC_{32}, respectively.

the above discussions, it is clear that our work has made an important contribution to superconductivity in graphene and will be of great interest to experimentalists working on Al-deposited graphene and related systems.

IV. CONCLUSION

In conclusion, the structural stability, electron-phonon properties, and superconductivity in Al-deposited graphene AlC_8 have been studied. The deposition of Al atoms can make the system to be in a metallic state. However, the structure is dynamically unstable but can be stabilized by hole doping.

The biaxial tensile strain was applied to study its effect on phonon and electron-phonon coupling. The low-energy in-plane modes of Al mixed with a small proportion of C out-of-plane modes contributes most to the electron-phonon coupling, and the high-energy in-plane C-C stretching modes also have appreciable contribution. With the increase of tensile strain, the high-energy phonon spectrum corresponding to the C-C stretching modes softens greatly and the electron-phonon coupling becomes stronger, resulting in the increase of superconducting transition temperature T_c to a value of more than 22 K, which is above the liquid hydrogen temperature of 20.3 K. Since it can be achieved within the experimentally

TABLE II. Bader charge (in units of $|e|$) for each atom in pristine AlC_8 unit cell. The atoms are labeled in Fig. 1(b).

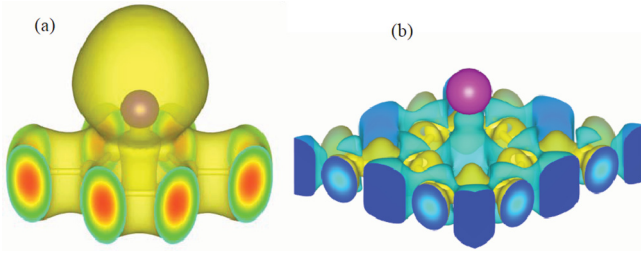| Atom	Al	C_1	C_2	C_3	C_4	C_5	C_6	C_7	C_8
Charge	2.270	4.150	4.150	4.150	4.150	4.150	4.150	3.915	3.915

FIG. 10. (a) Electron localization function and (b) charge density difference for pristine AlC_8 unit cell shown in Fig. 1(b). In (b), the color blue (yellow) represents the area where electrons are lost (obtained).

accessible doping and strain levels, the predicted Al-deposited graphene AlC_8 provides another platform for realizing superconductivity in graphene.

APPENDIX A: LATTICE STRUCTURE AND PHONON SPECTRA OF AlC_6, AlC_{24}, AND AlC_{32}

Besides AlC_8, other stoichiometries of Al and C, such as AlC_6, AlC_{24}, and AlC_{32}, were also studied. The total energies for each system under the lattice structures with hollow, top, and bridge coverages of Al atom on graphene were first investigated. Similarly to AlC_8, the hollow coverage also

shows the lowest energy for AlC_6, AlC_{24}, and AlC_{32}, with the relaxed lattice structures respectively shown in Figs. 9(a)–9(c). The corresponding phonon spectra for them are shown in Figs. 9(d)–9(f), from which the imaginary frequencies for certain low-energy modes can be seen, with the maximum of -116 cm^{-1}, -86 cm^{-1}, and -164 cm^{-1}, respectively. The absolute values of the maximum imaginary frequency for the three systems are larger than that of AlC_8, i.e., -58 cm^{-1}; thus they are more unstable. Especially, for AlC_6, with the same stoichiometric ratio as LiC_6 and CaC_6 [20–23], stabilization is very difficult. That is, whether doping electrons or holes, applying tensile or compressive strain to the system, the change of imaginary frequencies is very small. Thus, it cannot stably exist in reasonable experimental setups. Whether there is a geometry of Al-deposited graphene with no imaginary frequency in the phonon spectra is a question which is time-consuming and requires a lot of computing resources. This is still under investigation and is beyond the scope of the present work, and might be shown elsewhere in the future. For the case of AlC_8 under concern, we have proved that it is thermodynamically stable, and can be made dynamically stable by hole doping, and also be superconducting with T_c above the liquid hydrogen temperature under strain, which is an important supplement to the previous work on the electronic structure of AlC_8 [24], and also provides another platform for realizing superconductivity in graphene by depositing metal besides Li and Ca [20–23].

APPENDIX B: CHARGE PROPERTIES OF PRISTINE AlC_8

To know whether the Al atom forms bonds with the nearest C atoms, we calculated the Bader charge, electron localization function, and charge density difference for pristine AlC_8. The Bader charge for each atom in the AlC_8 unit cell is shown in Table II. The calculated Bader charges for the Al atom and the nearest C atoms (C_1 to C_6) are $2.270|e|$ and $4.150|e|$, respectively, indicating that Al loses electrons and the nearest C atoms gain electrons. The electron localization function of pristine AlC_8 in Fig. 10(a) shows the electron distribution in real space, showing the overlap between Al and the nearest C atoms. Moreover, to see more clearly the electron transfer and atom bonding, the charge density difference was calculated.
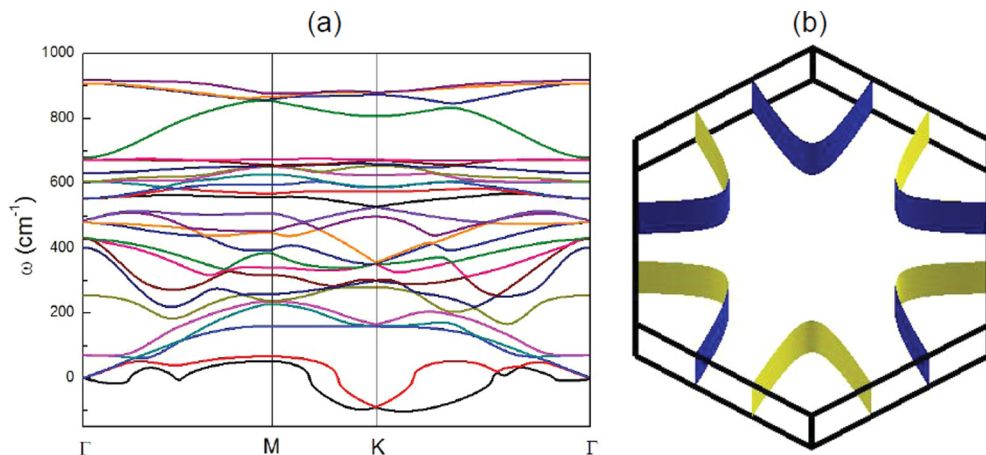

FIG. 11. (a) Phonon spectra and (b) Fermi surface of AlC_8 for the case of $p = 0.2$ and $\varepsilon = 15\%$.
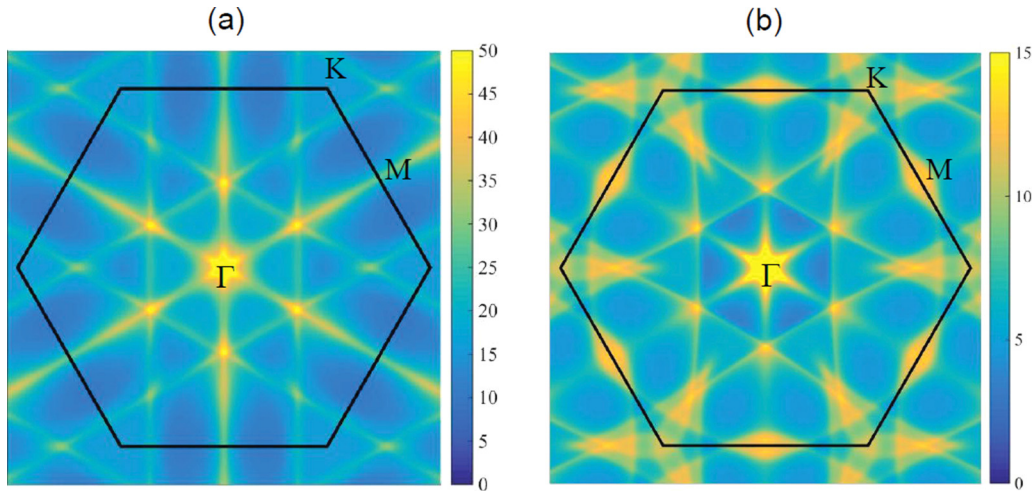
(a)

(b)

FIG. 12. Nesting functions for (a) the pristine case and (b) $p = 0.2$ and $\varepsilon = 15\%$ case.

It is defined as $\Delta\rho = \rho_{sys} - \rho_{gra} - \rho_{Al}$, in which ρ_{sys}, ρ_{gra}, and ρ_{Al}, respectively, represent the charge density of pristine AlC_8, graphene, and isolated Al atom. The calculated result is shown in Fig. 10(b); it is seen that electrons transfer from the bottom of Al atom to the graphene plane, especially to the middle of C-C bonds. Based on the above analysis, we conclude that Al forms bonds with the nearest C atoms.

APPENDIX C: ORIGIN OF THE LATTICE INSTABILITY OF AlC$_8$

For the lattice stability, we have found that the lattice for the pristine AlC_8 is unstable, with the phonon spectra shown in Fig. 2(a). The imaginary frequencies basically disappear with hole doping of $p = 0.2$. However, for the cases of hole doping level $p = 0.2$ and strain ε larger than 13%, the lattices are no longer stable. For example, here we show the phonon spectra of AlC_8 along high-symmetry line Γ-M-K-Γ for the case of $p = 0.2$ and $\varepsilon = 15\%$, which can be seen in Fig. 11(a). Along Γ-M, there is tiny phonon softening, whereas around K, there is significant softening of phonon modes along both M-K and K-Γ. By comparison, it is known that lead-halide perovskite structures such as $CH_3NH_3PbI_3$ show soft phonon modes at the Brillouin-zone boundary points R and M in the high-temperature cubic phase, which originates from the collective tilting of the PbI_6 octahedra [47]. A similar phenomenon was found in halide perovskites $CsSnI_3$ and $CsPbI_3$, in which doing linear response calculations at finite temperature can stabilize such phonon dispersion curves and remove the imaginary frequencies [48,49]. It is necessary to explore the possible origin of the lattice instability in AlC_8.

There are two most common mechanisms for the lattice instability: the electrostatic interaction and Kohn anomaly.

For dielectrics, the electrostatic interaction is the main reason, while for metals, the Kohn anomaly can also lead to the lattice instability. To explain the lattice instability of the pristine case as well as the $p = 0.2$ and $\varepsilon = 15\%$ case mentioned above, we calculate the Fermi surface nesting function for them. The Fermi surfaces are shown in Figs. 4(a) and 11(b), respectively. The nesting function can be obtained by

$$X(q) = \frac{1}{N} \sum_k \delta(\varepsilon_k - E_F)\delta(\varepsilon_{k+q} - E_F). \quad \text{(C1)}$$

Here N is the number of k points in the sum, ε_k and ε_{k+q} are the eigenvalues obtained by the first-principles calculations, and E_F is the Fermi energy. At the nonzero $X(q)$ points, the nesting effect of electrons in a metal can strongly influence atomic vibrations, and the phonon frequencies vary abruptly with q, which is a signature of the Kohn anomaly instability.

The calculated nesting functions for (a) the pristine case and (b) the $p = 0.2$ and $\varepsilon = 15\%$ case are shown in Fig. 12. From Fig. 12(a), it is seen that a strong nesting appears in the middle of Γ and M but not around K, which could not explain the imaginary frequency of phonon spectra along the K-M and K-Γ directions in Fig. 2(a). Thus, the lattice instability for the pristine case is not associated with the Kohn anomaly. We deduce that it originates from the electrostatic interaction induced by the abundant electrons provided by the Al atoms. It can be proved that the imaginary frequencies basically disappear by hole doping, as shown in Fig. 2(b). For the $p = 0.2$ and $\varepsilon = 15\%$ case, the nesting function in Fig. 12(b) shows nesting in the middle of Γ and M, and also around the K point, consistent with positions where the phonon softening occurs in the phonon spectra shown in Fig. 11(a). Thus, the instability of the lattice for this case mainly originates from the Kohn anomaly induced by the Fermi surface nesting effect.

[1] K. S. Novoselov, A. K. Geim, S. V. Morozov, D. Jiang, Y. Zhang, S. V. Dubonos, I. V. Grigorieva, and A. A. Firsov, Science **306**, 666 (2004).

[2] K. S. Novoselov, A. K. Geim, S. V. Morozov, D. Jiang, M. I. Katsnelson, I. V. Grigorieva, S. V. Dubonos, and A. A. Firsov, Nature (London) **438**, 197 (2005).

[3] A. K. Geim and K. S. Novoselov, Nat. Mater. **6**, 183 (2007).

[4] S. V. Morozov, K. S. Novoselov, M. I. Katsnelson, F. Schedin, D. C. Elias, J. A. Jaszczak, and A. K. Geim, Phys. Rev. Lett. **100**, 016602 (2008).

[5] A. H. Castro Neto, F. Guinea, N. M. R. Peres, K. S. Novoselov, and A. K. Geim, Rev. Mod. Phys. **81**, 109 (2009).

[6] V. N. Kotov, B. Uchoa, V. M. Pereira, F. Guinea, and A. H. Castro Neto, Rev. Mod. Phys. **84**, 1067 (2012).

[7] Y. Cao, V Fatemi, S. Fang, K. Watanabe, T. Taniguchi, E. Kaxiras, and P. Jarillo-Herrero, Nature (London) **556**, 43 (2018).

[8] Y. Cao, V. Fatemi, A. Demir, S. Fang, S. L. Tomarken, J. Y. Luo, J. D. Sanchez-Yamagishi, K. Watanabe, T. Taniguchi, E. Kaxiras, R. C. Ashoori, and P. Jarillo-Herrero, Nature (London) **556**, 80 (2018).

[9] A. Das, S. Pisana, B. Chakraborty, S. Piscanec, S. K. Saha, U. V. Waghmare, K. S. Novoselov, H. R. Krishnamurhthy, A. K. Geim, A. C. Ferrari, and A. K. Sood, Nat. Nanotechnol. **3**, 210 (2008).

[10] D. K. Efetov and P. Kim, Phys. Rev. Lett. **105**, 256805 (2010).

[11] K. Yokota, K. Takai, and T. Enoki, Nano Lett. **11**, 3669 (2011).

[12] B. Uchoa and A. H. Castro Neto, Phys. Rev. Lett. **98**, 146801 (2007).

[13] A. M. Black-Schaffer and S. Doniach, Phys. Rev. B **75**, 134512 (2007).

[14] R. Nandkishore, L. S. Levitov, and A. V. Chubukov, Nat. Phys. **8**, 158 (2012).

[15] C. Si, Z. Liu, W. Duan, and F. Liu, Phys. Rev. Lett. **111**, 196802 (2013).

[16] T. E. Weller, M. Ellerby, S. S. Saxena, R. P. Smith, and N. T. Skipper, Nat. Phys. **1**, 39 (2005).

[17] N. Emery, C. Hérold, M. D'astuto, V. Garcia, C. Bellin, J. F. Marêché, P. Lagrange, and G. Loupias, Phys. Rev. Lett. **95**, 087003 (2005).

[18] I. I. Mazin, Phys. Rev. Lett. **95**, 227001 (2005).

[19] M. Calandra and F. Mauri, Phys. Rev. Lett. **95**, 237002 (2005).

[20] G. Profeta, M. Calandra, and F. Mauri, Nat. Phys. **8**, 131 (2012).

[21] A. V. Fedorov, N. I. Verbitskiy, D. Haberer, C. Struzzi, L. Petaccia, D. Usachov, O. Y. Vilkov, D. V. Vyalikh, J. Fink, M. Knupfer, B. Büchner, and A. Grüneis, Nat. Commun. **5**, 3257 (2014).

[22] B. M. Ludbrook, G. Levy, P. Nigge, M. Zonno, M. Schneider, D. J. Dvorak, C. N. Veenstra, S. Zhdanovich, D. Wong, P. Dosanjh, C. Straßer, A. Stöhr, S. Forti, C. R. Ast, U. Starke, and A. Damascelli, Proc. Natl. Acad. Sci. USA **112**, 11795 (2015).

[23] J. Pešić, R. Gajić, K. Hingerl, and M. Belić, Europhys. Lett. **108**, 67005 (2014).

[24] S.-Y. Lin, Y.-T. Lin, N. T. T. Tran, W.-P. Su, and M.-F. Lin, Carbon **120**, 209 (2017).

[25] P. Giannozzi *et al.*, J. Phys.: Condens. Matter **21**, 395502 (2009); http://www.quantum-espresso.org.

[26] S. Baroni, S. de Gironcoli, and A. D. Corso, Rev. Mod. Phys. **73**, 515 (2001).

[27] G. Kresse and D. Joubert, Phys. Rev. B **59**, 1758 (1999).

[28] J. P. Perdew, K. Burke, and M. Ernzerhof, Phys. Rev. Lett. **77**, 3865 (1996).

[29] J. P. Perdew, A. Ruzsinszky, G. I. Csonka, O. A. Vydrov, G. E. Scuseria, L. A. Constantin, X. Zhou, and K. Burke, Phys. Rev. Lett. **100**, 136406 (2008).

[30] G. Henkelman, A. Arnaldsson, and H. Jónsson, Comput. Mater. Sci. **36**, 354 (2006).

[31] G. Kresse and J. Furthmüller, Phys. Rev. B **54**, 11169 (1996).

[32] G. M. Eliashberg, Zh. Eksp. Teor. Fiz. **38**, 966 (1960) [Sov. Phys. JETP **11**, 696 (1960)].

[33] P. B. Allen and R. C. Dynes, Phys. Rev. B **12**, 905 (1975).

[34] J. Zhou, Q. Sun, Q. Wang, and P. Jena, Phys. Rev. B **92**, 064505 (2015).

[35] D. F. Shao, R. C. Xiao, W. J. Lu, H. Y. Lv, J. Y. Li, X. B. Zhu, and Y. P. Sun, Phys. Rev. B **94**, 125126 (2016).

[36] E. S. Penev, A. Kutana, and B. I. Yakobson, Nano Lett. **16**, 2522 (2016).

[37] V. Zólyomi, N. D. Drummond, and V. I. Fal'ko, Phys. Rev. B **89**, 205416 (2014).

[38] Y. Ma, L. Kou, Y. Dai, and T. Heine, Phys. Rev. B **93**, 235451 (2016).

[39] C. A. Marianetti and H. G. Yevick, Phys. Rev. Lett. **105**, 245502 (2010).

[40] C. Si, W. Duan, Z. Liu, and F. Liu, Phys. Rev. Lett. **109**, 226802 (2012).

[41] C. Lee, X. Wei, J. Kysar, and J. Hone, Science **321**, 385 (2008).

[42] G. Csányi, P. Littlewood, A. H. Nevidomskyy, C. J. Pickard, and B. D. Simons, Nat. Phys. **1**, 42 (2005).

[43] B. Uchoa and Y. Barlas, Phys. Rev. Lett. **111**, 046604 (2013).

[44] B. Roy and V. Juričić, Phys. Rev. B **90**, 041413(R) (2014).

[45] V. J. Kauppila, F. Aikebaier, and T. T. Heikkilä, Phys. Rev. B **93**, 214505 (2016).

[46] F. Xu, P.-H. Chou, C.-H. Chung, T.-K. Lee, and C.-Y. Mou, Phys. Rev. B **98**, 205103 (2018).

[47] L. D. Whalley, J. M. Skelton, J. M. Frost, and A. Walsh, Phys. Rev. B **94**, 220301(R) (2016).

[48] C. E. Patrick, K. W. Jacobsen, and K. S. Thygesen, Phys. Rev. B **92**, 201205(R) (2015).

[49] A. Marronnier, H. Lee, B. Geffroy, J. Even, Y. Bonnassieux, and G. Roma, J. Phys. Chem. Lett. **8**, 2659 (2017).